



HAL
open science

Turbulence Anisotropy Carried by Streaks in the Neutral Atmospheric Surface Layer

Thomas Dubos, Philippe Drobinski, P. Carlotti

► **To cite this version:**

Thomas Dubos, Philippe Drobinski, P. Carlotti. Turbulence Anisotropy Carried by Streaks in the Neutral Atmospheric Surface Layer. *Journal of the Atmospheric Sciences*, 2008, 65 (8), pp.2631-2645. 10.1175/2007JAS2333.1 . hal-00311715

HAL Id: hal-00311715

<https://hal.science/hal-00311715v1>

Submitted on 25 Jan 2021

HAL is a multi-disciplinary open access archive for the deposit and dissemination of scientific research documents, whether they are published or not. The documents may come from teaching and research institutions in France or abroad, or from public or private research centers.

L'archive ouverte pluridisciplinaire **HAL**, est destinée au dépôt et à la diffusion de documents scientifiques de niveau recherche, publiés ou non, émanant des établissements d'enseignement et de recherche français ou étrangers, des laboratoires publics ou privés.

Turbulence Anisotropy Carried by Streaks in the Neutral Atmospheric Surface Layer

THOMAS DUBOS

Institut Pierre Simon Laplace, Laboratoire de Météorologie Dynamique, Palaiseau, France

PHILIPPE DROBINSKI

Institut Pierre Simon Laplace, Service d'Aéronomie, Paris, France

PIERRE CARLOTTI

Ministère de l'Équipement, Marseille, France

(Manuscript received 27 October 2006, in final form 27 June 2007)

ABSTRACT

The authors investigate the relationships between coherent structures and turbulence anisotropy in the neutral planetary boundary layer by means of empirical orthogonal function (EOF) analysis of large-eddy simulation (LES) data. The simulated flow contains near-surface transient streaks. The EOF analysis extracts the most energetic patterns from the velocity fluctuations based on their second-order spatial correlations. The scale and direction of streaks obtained from a level-by-level analysis of the LES flow field do correspond to that of the EOFs.

It is found that two characteristics of the turbulence anisotropy depend on whether or not the velocity fluctuations with a given horizontal wave vector present distinct patterns: (i) the vertical extent up to which the turbulent kinetic energy (TKE) is concentrated and (ii) the ratio of the vertical TKE E_V to the horizontal TKE E_H . Although still present in the complete signal, this anisotropy is strongly emphasized when the signal is projected onto the EOF structures. Hence the coherent structures do indeed carry more anisotropy than the remaining turbulent fluctuations. Furthermore, at horizontal wave vectors where energetic patterns are dominant, the ratio E_V/E_H takes values close to 0.2, representative of the ratio E_V/E_H based on the total LES flow and on in situ measurements.

1. Introduction

Important features of the near-surface turbulence in the neutrally stratified planetary boundary layer (NPBL) are a strong anisotropy and the presence of coherent structures (Moeng and Sullivan 1994; Carlotti 2002; Drobinski et al. 2004, 2007). Although each of these two features is well documented, the relationship between them, besides the fact that they both occur in the surface layer, has been less investigated. We present here such an investigation.

The present study deals with the NPBL and leaves the stable and unstable cases for future investigations. Near-neutral conditions are frequently met above very

rough surfaces such as forest and tall natural vegetation. Episodes of near-neutral conditions are also encountered over flat terrains as during the 1999 Cooperative Atmosphere–Surface Exchange Study (CASES-99) campaign. One of these episodes served for the validation of the numerical data analyzed in this work (Drobinski et al. 2007).

Sheared PBLs are populated with eddies, among which there are rolls and streaks. Rolls span the depth of the PBL and, once established, they persist for hours or even days (Etling and Brown 1993; Drobinski et al. 1998; Young et al. 2002). Because of their long duration, rolls are believed to be associated with the nonlinear saturation of normal-mode instabilities that reach a finite amplitude in a modified mean flow. Despite some variability, rolls form at angles to the mean wind above the NPBL compatible with such theories (Etling and Brown 1993). However, such rolls seldom form in large-eddy simulations (LES) of the NPBL

Corresponding author address: Dr. Thomas Dubos, Institut Pierre Simon Laplace, Laboratoire de Météorologie Dynamique, École Polytechnique, 91128 Palaiseau CEDEX, France.
E-mail: dubos@lmd.polytechnique.fr

(Moeng and Sullivan 1994). Instead, the near-surface flow is characterized by transient streaks, which are alternating bands of relatively higher and lower streamwise velocity and are responsible for a significant fraction of the surface stress. The streaks are spatially periodic elongated features of the NPBL that reside in the surface layer (SL) and lower portion of the outer-NPBL. Streaks appear to go through a continuous cycle of generation, growth, decay, and regeneration, and typical lifetimes of individual streaks are on the order of tens of minutes (Lin et al. 1996; Foster 1997; Drobinski and Foster 2003). They are thus different from the persistent PBL rolls. Streaks are also of much smaller scale (wavelengths $\approx 100\text{--}300$ m) than rolls. Because they align approximately along the mean shear corresponding to their vertical extent, streaks can form at larger angles to the mean wind above the NPBL than theoretical rolls (Young et al. 2002). Progress in high-resolution Doppler lidars now permits the in situ observation of streaks (Drobinski et al. 2004), which are the dominant feature of the near-surface flow in the NPBL.

Concomitant with the presence of streaks in the neutral SL, turbulence displays highly anisotropic characteristics: (i) the variances of the wind velocity fluctuations differ for the three components; that is, $\langle u^2 \rangle / u_*^2 \approx 5 - 6$, $\langle v^2 \rangle / u_*^2 \approx 3$ and $\langle w^2 \rangle / u_*^2 \approx 1 - 2$ (where $\langle \cdot \rangle$ stands for the time average, u , v and w are the streamwise, transverse, and vertical wind velocity fluctuation, and u_* is the friction velocity) or similarly $\langle v^2 \rangle / \langle u^2 \rangle$ and $\langle w^2 \rangle / \langle v^2 \rangle$ are about 0.5 as shown numerically (Moeng and Sullivan 1994; Drobinski et al. 2007) and experimentally (Panofsky 1974; Nicholls and Readings 1979; Grant 1986, 1992; Drobinski et al. 2004); (ii) close to the ground, the wind velocity spectra show a deviation from the $-5/3$ spectral slope expected for isotropic turbulence with the existence of a -1 power law at intermediate spectral subrange [e.g., Katul and Chu (1998) for a review and, more recently, Hunt and Morrison (2000), Hunt and Carlotti (2001), and Drobinski et al. (2004, 2007)].

In this paper we investigate the relationship between streaks and turbulence anisotropy in the near-surface flow of a well-resolved LES. One first issue is therefore to identify these streaks. Identifying the streaks is, however, only a first step, and to quantitatively evaluate their relationship with turbulence anisotropy we also want to know how much they contribute to various turbulent quantities like momentum fluxes. Hence a suitable coherent structure extraction technique has to be chosen. Indeed, while organized structures are frequently observed in numerical or field data, they have no unique definition and several identification tech-

niques coexist. In vortex identification methods, vortex cores are visualized as isosurfaces of eigenvalues of the velocity gradient, the pressure Hessian, and related tensors (Jeong and Hussain 1995). Conditional sampling is more quantitative in that it provides the flow and fluxes conditionally averaged with respect to the occurrence of some event, typically ejection or sweep events. Yet it is sometimes criticized on the grounds that the results depend on subjectively chosen sampling criteria. Many studies of PBL coherent structures have used conditional sampling and vortex visualization techniques (Lin et al. 1996; Foster et al. 2006). References to earlier studies can be found in Wilson (1996). Empirical orthogonal function (EOF) analysis, also known as principal component analysis (PCA) and proper orthogonal decomposition (POD), is an extraction technique which has been widely employed on engineering flows, especially the turbulent boundary layer over a smooth boundary (Berkooz et al. 1993). The outputs are the eigenfunctions of the correlation functions and are unique once a quadratic norm has been chosen. The method is generally considered more objective than other methods in the sense that arbitrary choices made by the investigator, such as defining thresholds, are reduced to a minimum. It is also a quantitative method since all quadratic quantities can be decomposed into contributions of the individual structures. Because of these properties, we chose the EOF analysis as our coherent structure extraction technique.

The possibilities of EOF analysis have been widely employed in the engineering context (Berkooz et al. 1993). In the geophysical context, EOF analysis is also widely used in climatic variability studies but less so in boundary layer meteorology, possibly because of the large datasets required by the method. A few studies are based on an EOF analysis of PBL or PBL-like data (Preisendorfer 1988), and follow the progress in the availability of detailed data. While early studies were limited to a one-dimensional (Jallickee and Ropelewski 1979) or two-dimensional analysis, increasing computing power and data availability recently enabled three-dimensional EOF analysis in the convective PBL (Rinker and Young 1996; Wilson 1996), the neutral PBL (Esau 2003), or in a wheat canopy (Finnigan and Shaw 2000). Still, reliable three-dimensional data in the neutral SL became available only recently and this work elaborates on this progress (Carlotti 2002; Drobinski et al. 2007). Beyond the extraction and identification of coherent structures, which is the principal aim of these works, EOF analysis also permits to study the contribution of the structures to the flow energetics (Wilson and Wyngaard 1996). Wilson and Wyngaard (1996) analyzed a LES simulation of a weakly convec-

tive PBL in a mesoscale box relevant for rolls spanning most of the PBL. However, the resolution of this simulation was too coarse to study the SL. To focus on the SL streaks, we analyze a more finely resolved LES in a smaller box (Carlotti 2002), extract coherent structures, and proceed with the analysis of their contribution to turbulence anisotropy.

Because of horizontal homogeneity, the EOF analysis extracts the most energetic vertical pattern for each horizontal wave vector. As a result, the corresponding flows have the same structure as the linear normal modes or optimal perturbations and can be compared to them. Furthermore, two aspects of anisotropy can be investigated: (i) the vertical–horizontal ratio of the velocity components and of the extracted flow patterns and (ii) the dependence of turbulent quantities on the orientation of the horizontal wave vector relatively to the geostrophic wind. The present work complements that of Foster et al. (2006), which was based on conditional sampling of the same dataset. Conditional sampling does not separate the various horizontal scales of the velocity fluctuations; conversely EOF analysis does not distinguish between ejections and sweeps. This makes the two methods complementary in that they focus on different issues.

Section 2 presents the basis of the data analysis technique. Section 3 describes the individual structures and section 4 investigates their relationship with the anisotropy. Section 5 summarizes the results.

2. Data analysis

a. The dataset

We use the nonhydrostatic LES code Meso-NH (Lafore et al. 1998) to model a NPBL in a box with size $(L, l, H) = 3 \text{ km} \times 1 \text{ km} \times 750 \text{ m}$ along the $x, y,$ and z axes, respectively. The mesh cell is a cube of side 6.25 m ($N_x \times N_y \times N_z = 480 \times 160 \times 120$) to avoid any grid-induced anisotropy. The subgrid-scale (SGS) model is based on a turbulent kinetic energy (TKE) equation (Cuxart et al. 2000). Near the ground, the results may be sensitive to different SGS schemes. To estimate this sensitivity, two additional LES were performed with different SGS schemes: a modified mixing length model by Redelsperger et al. (2001) and Smagorinsky's model (Smagorinsky 1963). However, the simulated flow proved not to be very dependent on the SGS model except less than 20 m (3 grid cells) above ground (Drobinski et al. 2007). The computational box is assumed to be at midlatitude, and a large-scale pressure gradient that would balance a geostrophic wind of 10 m s^{-1} above the NPBL is imposed. The top of the domain is a rigid lid, a legitimate approximation as long

as there is no interest in the dynamics near the inversion layer capping the PBL (Andren et al. 1994; Hess 2004). The lateral boundary conditions are periodic. At the first grid point above the surface ($z = 3.125 \text{ m}$), the wind speed equals $(u_*/\kappa) \log(z/z_0)$ where u_* is the friction velocity, $\kappa = 0.4$ is the von Kármán constant, and $z_0 = 10 \text{ cm}$ is the roughness length.

The simulation was started from a laminar velocity field in which a very weak random temperature fluctuation ($\Delta T/T \approx 3 \times 10^{-4}$) was imposed at the bottom of the domain in order to generate turbulence. The temperature fluctuations were quickly damped, resulting in a neutrally stratified turbulent flow. After 10 h of physical time, 14 snapshots of the three-dimensional velocity, pressure, and the TKE were extracted and stored, with 500 s between each snapshot. The 500-s interval between snapshots is comparable to the mean advection time across the domain, and the flow statistics do not change appreciably between snapshots, indicating that the flow has reached statistical equilibrium. For example, the standard deviation of the mean friction velocity, $u_* = 0.42 \text{ m s}^{-1}$, between the snapshots is $\delta u_* = 0.0034 \text{ m s}^{-1}$, less than 1%.

We decompose the velocity field into a mean flow $[U(z), V(z), 0]$ forced by large-scale pressure gradient and turbulent fluctuations $[u(x, y, z, t), v(x, y, z, t), w(x, y, z, t)]$. In the time-averaged wind hodograph (Fig. 1) the wind is oriented about 12° left to the x direction in high layers and about 20° left to the x direction close to the ground, following an Ekman spiral continued by a logarithmic layer near the surface. The mean speed profile is approximately logarithmic up to about 270 m. However, there is no appreciable turning in the profile only up to about 40 m, which we take to be the top of the surface layer. In the first 100 m, the wind fluctuations form streaky structures roughly aligned with the ground wind. These structures appear clearly on horizontal cross sections of the velocity field (Fig. 2) and are the dominant features near the surface, associated with an overturning circulation, for example, alternating bands of updrafts and downdrafts approximately centered on the streaks (Foster et al. 2006). The spacing of the streaks has several apparent scales, from $\sim 100\text{-m}$ spacing near the surface to $\sim 200\text{-m}$ spacing higher up. The structure of the streaks is broadly consistent with most LES of the neutrally stratified PBL (e.g., Dardorff 1972; Moeng and Sullivan 1994; Lin et al. 1996; Drobinski and Foster 2003). These instantaneous flow realizations show a coherent organization of the simulated turbulence that is not purely periodic but is an aggregation of smaller-scale structures.

Figure 3 shows the variances normalized by u_*^2 , as a function of height. The normalized variances $\langle u^2 \rangle / u_*^2$,

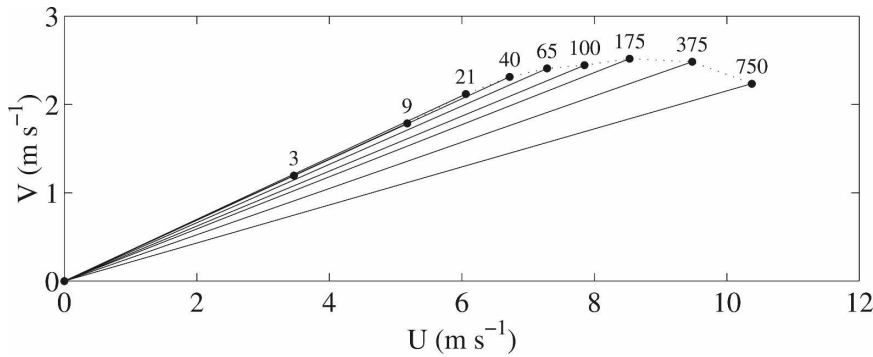


FIG. 1. Hodograph of mean wind, time-averaged after reaching statistical equilibrium. Various heights above the surface are marked. The total PBL height is $H = 750$ m.

$\langle v^2 \rangle / u_*^2$ and $\langle w^2 \rangle / u_*^2$ are about 5–6, 3, and 1–2 up to about $0.13H$ (i.e., 100 m) as in Panofsky (1974). The ratios of $\langle v^2 \rangle / \langle u^2 \rangle$ and $\langle w^2 \rangle / \langle v^2 \rangle$ are about 0.5 which is in good agreement with LES studies (Moeng and Sullivan 1994) and observations (Nicholls and Readings 1979; Grant 1986, 1992; Drobinski et al. 2004). These ratios tend to 1 near the PBL top.

The results of this LES were compared to theoretical developments for two-point statistics (Carloti 2002) and integral length scales (Carloti and Drobinski 2004)

near the ground and were validated against sonic anemometer and Doppler lidar measurements in the near-neutral surface layer collected on 13 October 1999 during the CASES-99 campaign (Drobinski et al. 2007). The comparison between the LES and the observations reveals good agreement for the vertical profiles of wind speed, momentum flux, and wind component variances as well as the near-surface flow pattern.

We now expose how the EOF analysis permits to recover energetic patterns from this complex signal.

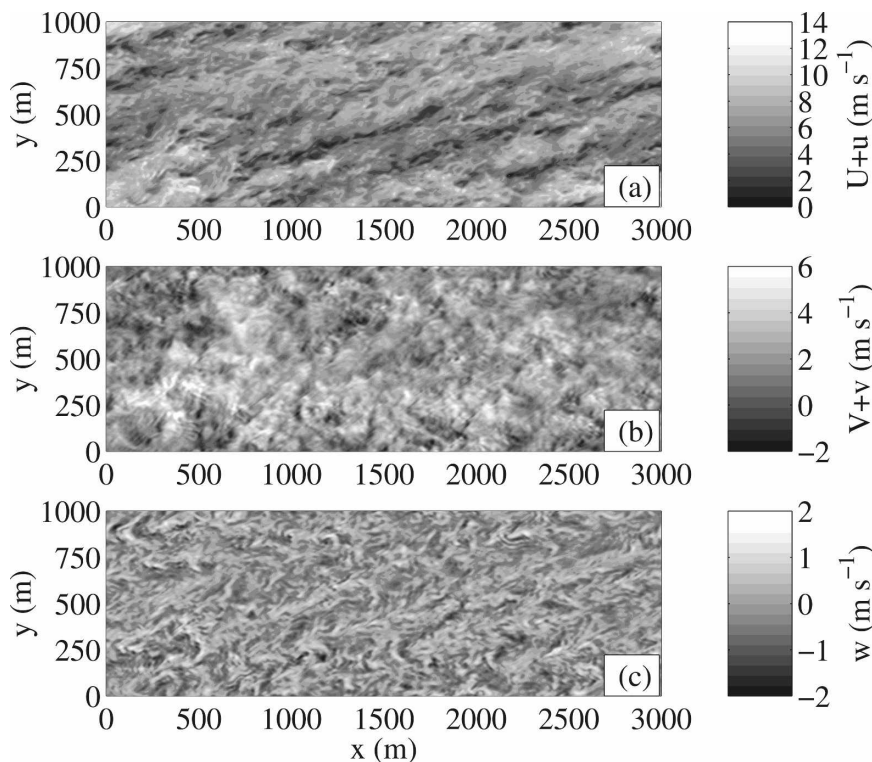


FIG. 2. Snapshot of the three velocity components $U + u$, $V + v$, and w in m s^{-1} at altitude $z = 60$ m.

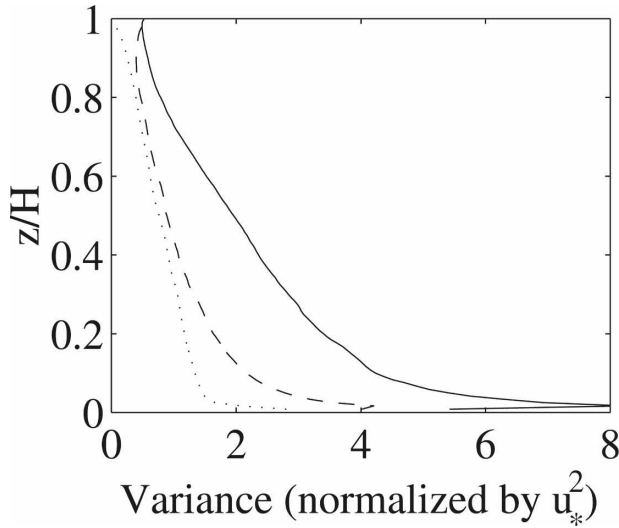


FIG. 3. Vertical profiles of normalized variances $\langle u^2 \rangle / u_*^2$ (solid line), $\langle v^2 \rangle / u_*^2$ (dashed line), and $\langle w^2 \rangle / u_*^2$ (dotted line) as a function of height.

b. Principle of EOF analysis

For completeness, we summarize the basic steps of the method and the most important properties of its outcome. An application of the method to the weakly convective PBL is described in Wilson (1996) and more details can be found in Berkooz et al. (1993) and Holmes et al. (1996).

In the sequel, we use small letters for time-dependent quantities and capital or Greek letters for statistical quantities and the quantities derived from them. We also use the superscript and the index i to number the EOFs and derived quantities. The subscript and indexes j, k are used for the three components of the velocity vector. The indexes m and n correspond to the horizontal wave vector.

$$\langle \|\mathbf{u}(t) - a^1(t)\phi^1\|^2 \rangle = \langle \|\mathbf{u}(t)\|^2 \rangle - \langle [a^1(t)]^2 \rangle \quad \text{with}$$

$$\langle [a^1(t)]^2 \rangle = \langle [\mathbf{u}(t), \phi^1]^2 \rangle = \iint R_{jk}(x, x', y, y', z, z') \phi_j^1(x, y, z) \phi_k^1(x', y', z') \frac{dx dx'}{L^2} \frac{dy dy'}{l^2} \frac{dz dz'}{H^2}, \quad (3)$$

where R_{jk} is the self-correlation function

$$R_{jk}(x, x', y, y', z, z') = \langle u_j(x, y, z; t) u_k(x', y', z'; t) \rangle. \quad (4)$$

We have the freedom to choose ϕ^1 such as to minimize the error. Introducing the Lagrange multiplier κ^1 associated to the constraint $\langle \phi^1, \phi^1 \rangle = 1$ and setting to zero

1) EIGENVALUE PROBLEM

We consider the time series of the state vector $\mathbf{u}(t)$, where \mathbf{u} is the deviation of the three-dimensional velocity field from its time average; for example

$$\begin{aligned} u_1(x, y, z; t) &= u(x, y, z, t) \\ u_2(x, y, z; t) &= v(x, y, z, t) \\ u_3(x, y, z; t) &= w(x, y, z, t). \end{aligned}$$

We define $\langle \rangle$ to be the time average over the duration of the simulation. The purpose of the EOF analysis is to find special state vectors (ϕ^1, \dots, ϕ^N) , called empirical orthogonal functions, that form an orthonormal basis and optimally represent $\mathbf{u}(t)$ in the least squares sense. For this we first need a definition of the Euclidean norm $\|\mathbf{u}\|$ of a state vector, or equivalently a scalar product $[\mathbf{u}(t), \mathbf{u}(t')]$ between two state vectors. It is common to choose (\mathbf{u}, \mathbf{u}) on energetic grounds (Berkooz et al. 1993), and we define (\mathbf{u}, \mathbf{u}) to be proportional to the volume-averaged TKE:

$$\begin{aligned} \|\mathbf{u}\|^2 = (\mathbf{u}, \mathbf{u}) &= \frac{1}{LlH} \int (u^2 + v^2 + w^2) dx dy dz \\ &= \frac{1}{LlH} \int u_j u_j dx dy dz, \end{aligned} \quad (1)$$

where the summation over the repeated indices (here $j = 1 \dots 3$) is implied.

Consider first the one-dimensional space spanned by ϕ^1 . For a given state $\mathbf{u}(t)$, the best approximation of $\mathbf{u}(t)$ by a multiple of ϕ^1 is $a^1(t)\phi^1$, where

$$a^1(t) = [\phi^1, \mathbf{u}(t)] = \frac{1}{LlH} \int \phi_j^1(x, y, z) u_j(x, y, z, t) dx dy dz. \quad (2)$$

The coefficient $a^1(t)$ is called the score of the sample $\mathbf{u}(t)$ with respect to ϕ^1 . The error we commit by projecting $\mathbf{u}(t)$ onto ϕ^1 is on average

the first variation of $\kappa^1(\phi^1, \phi^1) - \langle a^1(t)^2 \rangle$ with respect to ϕ^1 , we find that the optimal ϕ^1 is a solution of the eigenproblem:

$$\begin{aligned} \frac{1}{LlH} \int R_{jk}(x, x', y, y', z, z') \phi_k^1(x', y', z') dx' dy' dz' \\ = \kappa^1 \phi_j^1(x, y, z). \end{aligned} \quad (5)$$

If we now search for the subspace (ϕ^1, \dots, ϕ^N) onto which the orthogonal projection of the signal produces the least error, we arrive at the same eigenproblem, each EOF ϕ^i being associated with its own eigenvalue κ^i . A global minimum of the error is realized if $\kappa^1, \dots, \kappa^N$ are the N largest eigenvalues of the self-correlation

function. Hence the first EOF ϕ^1 is associated to the largest eigenvalue κ^1 , the second EOF to the second largest, and so on.

Notice that the scores $a^i(t)$ with respect to different EOFs of index i and i' have a vanishing correlation:

$$\begin{aligned} \langle a^i(t)a^{i'}(t) \rangle &= \int \int R_{jk}(x, x', y, y', z, z') \phi_j^i(x, y, z) \phi_k^{i'}(x', y', z') \frac{dx dx'}{L^2} \frac{dy dy'}{l} \frac{dz dz'}{H^2} \\ &= \kappa^{i'} \int \phi_j^i(x, y, z) \phi_j^{i'}(x, y, z) \frac{dx dy dz}{L l H} = \kappa^{i'} (\phi^i, \phi^{i'}) = 0 \quad \text{if } i \neq i'. \end{aligned} \tag{6}$$

Furthermore $\langle a^i(t)^2 \rangle = \kappa^i$. The eigenvalue κ^i is therefore called the energy explained by the i -th EOF.

2) EFFECT OF STATISTICAL HOMOGENEITY

Because of periodic boundary conditions in the x and y directions, it is convenient to write the velocity field in Fourier representation:

$$u_j(x, y, z, t) = \text{Re} \sum_{m,n} \hat{u}_j(m, n, z, t) \exp 2i\pi \left(\frac{mx}{L} + \frac{ny}{l} \right), \tag{7}$$

where the horizontal wave vector $(k_x, k_y) = 2\pi(m/L, n/l)$ is quantized according to the box dimensions L and l . With this normalization,

$$(\mathbf{u}, \mathbf{u}) = \frac{1}{H} \int \sum_{m,n} \hat{u}_j(m, n) \hat{u}_j^*(m, n) dz, \tag{8}$$

where the star * stands for complex conjugation. Repeating the above steps, the eigenproblem satisfied by $\hat{\phi}^i$ is

$$\frac{1}{H} \int \sum_{m',n'} \hat{R}_{jk}(m, m', n, n', z, z') \hat{\phi}_k^i(m', n', z') dz' = \kappa^i \hat{\phi}_j^i(m, n, z), \quad \text{where} \tag{9}$$

$$\hat{R}_{jk}(m, m', n, n', z, z') = \langle \hat{u}_j(m, n, z; t) \hat{u}_k^*(m', n', z'; t) \rangle. \tag{10}$$

If the statistics are invariant under horizontal translations, the cross correlation $\hat{R}_{jk}(m, m', n, n', z, z')$ between different wave vectors is zero. The different wave vectors are then decoupled in the above eigenproblem and it is sufficient to solve, independently for each mode (m, n) ,

$$\begin{aligned} \frac{1}{H} \int \hat{R}_{jk}(m, m, n, n, z, z') \hat{\phi}_k^i(m, n, z') dz' \\ = K^i(m, n) \hat{\phi}_j^i(m, n, z), \end{aligned} \tag{11}$$

where we have noted $K^i(m, n)$ the energy explained by the i -th EOF $\hat{\phi}_j^i(m, n, z)$.

3) DISCRETIZATION AND PRACTICAL STEPS

In practice a number p of snapshots at times t_1, \dots, t_p is used and the time average is computed as the average over the snapshots.

In addition, we reshape the triple profile $\hat{u}_j(m, n, z; t)$ into a single vector \hat{g}_j of length $3N_z$:

$$\hat{g}_{3k+j}(m, n; t) = \hat{u}_j(m, n, z_k; t), \tag{12}$$

$$\hat{\gamma}_{3k+j}^i(m, n) = \hat{\phi}_j^i(m, n, z_k), \tag{13}$$

where the z_k are the altitudes of the N_z vertical levels. Consistently with the uniform grid, the eigenproblem (11) may be approximated by

$$\frac{1}{N_z} C_{jk}(m, n) \hat{\gamma}_k^i(m, n) = K^i(m, n) \hat{\gamma}_j^i(m, n), \tag{14}$$

where $C_{jk}(m, n)$ is the self-correlation matrix:

$$\begin{aligned} C_{jk} &= \langle \hat{g}_k(m, n; t) \hat{g}_k^*(m, n; t) \rangle \\ &= \frac{1}{p} \sum_{q=1}^p \hat{g}_k(m, n; t_q) \hat{g}_k^*(m, n; t_q). \end{aligned} \tag{15}$$

Each of the p snapshots is first Fourier transformed in order to obtain $\hat{u}_j(m, n, z; t)$. We then proceed inde-

pendently for each mode (m, n) . We construct $\hat{g}_k(m, n; t)$ according to definition (12) then compute $C_{kk}(m, n)$ according to (15). We solve the eigenvalue problem (14) with a standard linear algebra package and obtain the eigenvalues $K^i(m, n)$ and eigenvectors $\hat{\gamma}_k^i(m, n)$. Finally the three profiles $\hat{\phi}_j^i(m, n, z)$ defining the i -th EOF are reconstructed using (13). We store all eigenvalues and the first two EOFs for further reference.

Our set of realizations consists of 14 snapshots of the whole velocity field taken at different instants. Thus this procedure extracts the energetic spatial flow patterns and drops any temporal correlations from the signal. Furthermore the number of EOFs is equal to the dimension of the space spanned by the signal, here 14 because of the small size of our sample. We checked that this number of samples is nevertheless sufficient for the present study by performing the statistical analysis twice, once with the complete set of 14 samples and once with only the first 7 samples. We found insignificant differences in the quantities analyzed in the sequel, and especially those presented in section 4.

c. Energy-weighted decomposition

At each wave vector, we compute the ratio $K^1(m, n)/K(m, n)$, where $K(m, n) = \sum_i K^i(m, n)$ is the contribution of the Fourier mode (m, n) to the vertically

integrated TKE. This ratio is the energy fraction explained by the first ($i = 1$) EOF and takes values between 0 and 1. Suppose for instance that for a given wave vector $K^i(m, n)/K(m, n) = 1$. In this case all scores $a^i(t)$ with $i > 1$ are zero. Thus the flow (within this Fourier mode) has the same vertical structure at all instants given by $\text{Re}\{\hat{\phi}_j^1(m, n, z) \exp 2i\pi[(mx/K) + (ny/l)]\}$, but appears with a random amplitude given by $|a^1(t)|$ and at a random position given by the phase of $a^1(t)$. Conversely, if the energy is equipartitioned among all EOFs, the signal is white-in-space noise. So only wave vectors where the first EOF explains an important fraction of the energy present distinct patterns and can be said to be “strongly structured.” Conversely, wave vectors with a low fraction of energy explained by the first EOF correspond, from the point of view of the EOF analysis, to more disordered motions.

Because of the statistical orthogonality of the scores $a^i(t)$, any quantity that depends quadratically on the velocity fluctuations can, on average, be split into individual contributions from the EOFs. Quadratic quantities of particular interest here are the turbulent kinetic energy and the shear production of turbulent kinetic energy. The horizontally averaged turbulent kinetic energy $e(z, t)$ and shear production $s(z, t)$ can first be written as the sum of contributions from each Fourier mode:

$$\begin{aligned}
 e(z, t) &= \iint (u^2 + v^2 + w^2) \frac{dx dy}{2Ll} = \sum_{mn} e(m, n, z, t), \quad \text{where } e(m, n, z, t) = \frac{\hat{u}_j(m, n, z, t)\hat{u}_j^*(m, n, z, t)}{2} \\
 s(z, t) &= \iint w \left(u \frac{dU}{dz} + v \frac{dV}{dz} \right) \frac{dx dy}{Ll} = \sum_{mn} s(m, n, z, t), \quad \text{where} \\
 s(m, n, z, t) &= \text{Re} \left\{ \left[\hat{u}(m, n, z, t) \frac{dU}{dz} + \hat{v}(m, n, z, t) \frac{dV}{dz} \right]^* \hat{w}(m, n, z, t) \right\}. \tag{16}
 \end{aligned}$$

On average, the quadratic quantities may be further decomposed as energy-weighted contributions from the individual EOFs:

$$E(m, n, z) = \sum_i K^i(m, n) E^i(m, n, z), \tag{17}$$

with $E(m, n, z) = \langle e(m, n, z, t) \rangle$ \tag{18}

and $E^i(m, n, z) = \frac{|\hat{\phi}_1^i(z)|^2 + |\hat{\phi}_2^i(z)|^2 + |\hat{\phi}_3^i(z)|^2}{2}$, \tag{19}

$$\langle s(m, n, z, t) \rangle = \sum_i K^i(m, n) S^i(m, n, z)$$

where $S^i(m, n, z)$

$$= \text{Re} \left\{ \left[\hat{\phi}_1^i(m, n, z) \frac{dU}{dz} + \hat{\phi}_2^i(m, n, z) \frac{dV}{dz} \right]^* \hat{\phi}_3^i(m, n, z) \right\}.$$

It follows finally that the profiles of TKE and TKE production $\langle e(z, t) \rangle$ and $\langle s(z, t) \rangle$ can be expressed as sums over the spectral domain (indexes m, n) and over the sequence of EOFs (index i) weighted by the energy explained by each EOF:

$$\langle e(z, t) \rangle = \sum_{i,m,n} K^i(m, n) E^i(m, n, z), \tag{20}$$

$$\langle s(z, t) \rangle = \sum_{i,m,n} K^i(m, n) S^i(m, n, z). \tag{21}$$

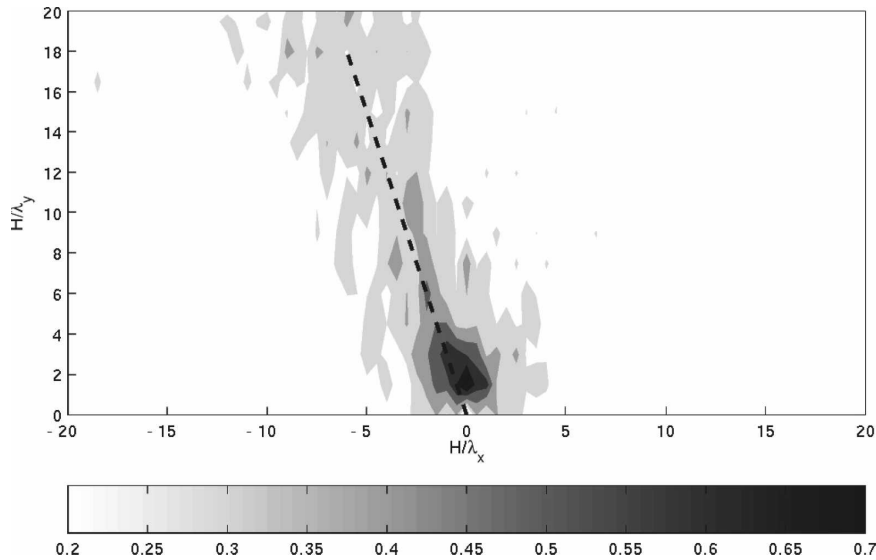


FIG. 4. Energy fraction $K^1(m, n)/K(m, n)$ explained by the first EOF of each Fourier mode as a function of the normalized wave vector $H\mathbf{k}/2\pi = (H/\lambda_x, H/\lambda_y) = H(m/L, n/l)$, where $H = 750$ m is the PBL height.

In decompositions (20) and (21), it can be informative to compute and compare partial sums, where the triplet of indexes (i, m, n) spans only a subset of all possible indices, for instance the subset $D = \{(i, m, n); i = 1\}$ containing, at each wave vector (m, n) , only the most energetic EOF ($i = 1$):

$$\begin{aligned} \langle e(z, t) \rangle_D &= \sum_{(i, m, n) \in D} K^i(m, n) E^i(m, n, z) \\ &= \sum_{m, n} K^1(m, n) E^1(m, n, z), \end{aligned} \quad (22)$$

$$\begin{aligned} \langle s(z, t) \rangle_D &= \sum_{(i, m, n) \in D} K^i(m, n) S^i(m, n, z) \\ &= \sum_{m, n} K^1(m, n) S^1(m, n, z). \end{aligned} \quad (23)$$

Contributions of other subsets will be considered in the next subsection.

3. Energetic weight and flow structure of the extracted patterns

a. Energetic EOFs

We display in Fig. 4 the energy fraction $K^1(m, n)/K(m, n)$ explained by the first ($i = 1$) EOF at each wave vector. Notice that we normalize the length scales by the PBL depth H . We could have chosen the depth of the SL as a characteristic length scale, but since it scales with the PBL depth (Holtstlag and Nieuwstadt 1986)

both choices are sensible. Furthermore, since the PBL depth is more frequently directly available than the SL depth, normalizing by H makes it easier to compare with existing or future literature.

As explained before, the wave vector presents distinct patterns if the energy fraction explained by the first EOF is large. We shall call such wave vectors strongly structured. The choice of a threshold is somewhat arbitrary but does not affect the overall shape of the spectral domain where wave vectors are strongly structured: wave vectors where the first EOF explains a large fraction of the energy lie in a narrow range of the Fourier space close to the line $m + n = 0$, or, equivalently, $3k_x + k_y = 0$ [remember that $(k_x, k_y) = 2\pi(m/L, n/l)$ and that the domain is rectangular with $L = 3l$]. Actually, the wave vector where the energy fraction explained by the first EOF is maximum lies off this line at $(m, n) = (0, 2)$. However, since it corresponds to a very grave mode with only two wavelengths fitting in the computational domain, it is suspect of finite-size effects. Hence we shall not discuss this mode specifically and will concentrate on the line $3k_x + k_y = 0$. This line corresponds to a phase line at an angle of as in $(1/3) \sim 19.5^\circ$ with respect to the x axis, almost parallel to the surface wind, which is at about 20° with respect to the x axis (Fig. 1). Hence the extracted coherent structures have the same orientation as found from the level-by-level identification of streaks (Fig. 2).

To quantify in more detail the energetic weight of the extracted structures, we now consider several contributions to the profiles of TKE and of shear production of

energy. The first contribution, already defined, is due to the dominant EOF of each horizontal wave vector:

$$D = [(i, m, n): i = 1]. \tag{24}$$

We also define the set S of indexes whose horizontal wave vector is strongly structured as obtained above; that is,

$$S = [(i, m, n): m + n = 0]. \tag{25}$$

Finally, it is natural to consider the contribution of those indexes that correspond both to a strongly structured wave vector and a dominant EOF:

$$S \cap D = [(i, m, n): i = 1 \text{ and } m + n = 0]. \tag{26}$$

We display the contributions of sets S , D , and $S \cap D$ to the vertical profiles of turbulent kinetic energy and of shear production of energy (Fig. 5).

Let us first consider the contribution of set S of strongly structured wave vectors. This contribution (circles) is an order of magnitude smaller than the complete average (solid), because strongly structured wave vectors cover only a very small fraction of the spectral space. Next, it is interesting to compare the contribution due to set D (dominant EOFs) to the complete average. This contribution (crosses) is now 2–3 times smaller than the complete average (solid). Indeed most wave vectors are weakly structured (do not present distinct patterns); hence, by ignoring all but one EOF at each wave vector, we also drop a lot of the velocity fluctuations. Let us finally compare the contributions due to sets S and $S \cap D$. By definition, the set $S \cap D$ is made of the most energetic EOFs of set S , the set of strongly structured wave vectors. Now, although set $S \cap D$ (dots) consists of much fewer EOFs than S (circles), both contribute by a comparable amount.

Hence the EOFs, at strongly structured wavenumbers, are the major contributor not only to the TKE but also to other quadratic quantities such as the production of TKE by shear. However strongly structured wavenumbers represent a small fraction of the total TKE. As a result, when focusing on the properties of the EOFs, care should be taken that these properties are representative of the total flow. The contribution of the coherent structures can then be assessed by comparing the properties of the coherent structures and of the total flow. This will be our methodology in section 4.

b. Typical flow structure

The dynamical origin of the rolls and streaks has been investigated in idealized models of the NPBL, especially the Ekman flow. Lilly established that the Ek-

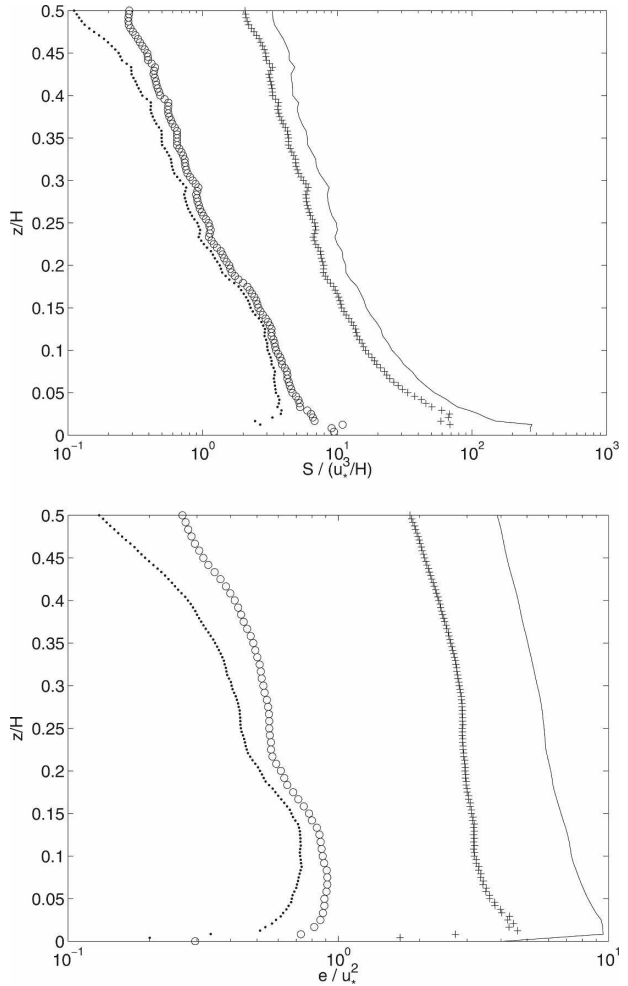


FIG. 5. Profiles of (top) turbulent kinetic energy $E(z)$ and (bottom) shear production of energy $S(z)$ as a function of the altitude z normalized by the PBL height $H = 750$ m: complete average (solid) and contributions of sets S (strongly structured wave vectors; circles), D (dominant EOFs; crosses), and $S \cap D$ (dots).

man flow is subject to an inflexion point instability (Lilly 1966). The rolls observed in the near-neutral PBL are usually interpreted as the outcome of this instability. More recently, Foster pointed out that optimal perturbations of the Ekman flow present large transient amplifications and that their scale and orientation are in broad agreement with those of near-surface streaks (Foster 1997). These analyses based on linearized dynamics lack, however, all of the nonlinear mechanisms that support turbulence. Especially, the decay of streaks appears to be a nonlinear process (Drobinski and Foster 2003). Nevertheless, it is interesting to compare the flow patterns emerging from these idealized studies to those extracted from this complex flow obeying fully nonlinear dynamics.

Indeed, because of incompressibility, the flow corre-

sponding to a single Fourier mode or to several Fourier modes with parallel wave vectors can be conveniently described in terms of an across-wave vector horizontal (along streak) velocity u' and an along-wave vector streamfunction, from which the vertical velocity w and the along-wave vector horizontal velocity v' are derived. This description and choice of axes is called Squire's transformation in the context of normal-mode stability analysis. This common flow structure between EOFs, unstable normal modes, and optimal perturbations is what makes the comparison straightforward.

We find that the first EOFs are concentrated close to the ground with a vertical extension comparable to their horizontal wavelength. At very low wavenumbers ($-m = n = 1, 2$, not shown), the vertical scale of the EOFs is about $200 \sim 400$ m. No streaks are distinguishable on horizontal cross sections of the velocity field at such altitudes. Furthermore, the corresponding horizontal scale

$$\lambda = (\lambda_x^{-2} + \lambda_y^{-2})^{-1/2} = (m^2/L^2 + n^2/l^2)^{-1/2} \quad (27)$$

is $\lambda = 474$ m for $-m = n = 2$ ($L = 3$ km, $l = 1$ km). Such large horizontal scales comparable to the domain size are probably affected by finite-size effects, as well as the mode $(m, n) = (0, 2)$ where the explained energy fraction is maximal. Hence higher-wavenumber EOFs ($-m = n = 4, 5$, $\lambda = 237$ m, 190 m), displayed in Fig. 6, are more likely to correspond reliably to the streaks. Since the EOFs are defined through the eigenproblem (14) up to a multiplicative constant (in the computations the constant is determined by the convention that the EOF has unit energy), the units of Fig. 6 are arbitrary. Both EOFs have the structure of an alternating along-streak jet superimposed onto two counterrotating rolls typical of linearly unstable normal modes and of optimal perturbations (Foster 1997). The streamfunction is approximately in quadrature with respect to the along-streak velocity. This means that the along-streak and vertical velocities are roughly in phase, producing, on average, a vertical flux of horizontal momentum and extracting energy from the mean shear. Compared to the along-streak velocity, the streamfunction of the linearly most unstable normal mode extends vertically roughly twice as much (Foster 1997, Fig. 4). At contrast, the along-streak velocity and streamfunction of the optimal perturbations have roughly the same vertical extent (Foster 1997, Figs. 7–8). In the patterns displayed in Fig. 6, the streamfunction and the along-streak velocity present comparable vertical extents. Thus, the first EOF bears more resemblance to the optimal perturbation than to the unstable normal mode.

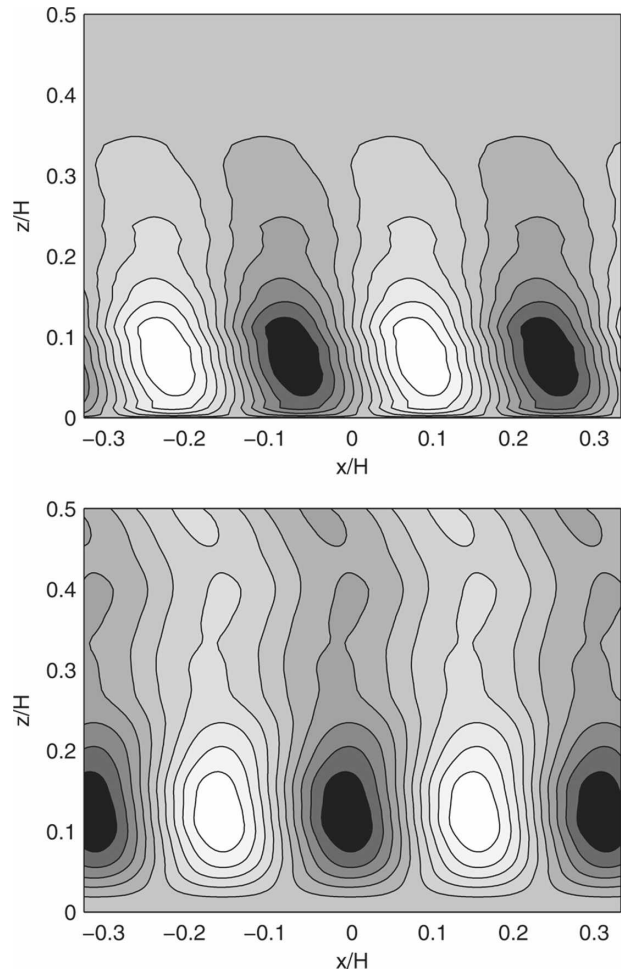


FIG. 6. Flow structure of the first EOF at wave vector $\mathbf{k} = 2\pi(-4/L, 4/l)$, corresponding to a horizontal-scale $\lambda = 237$ m and phase lines almost parallel to the surface wind. The streak axis is perpendicular to the plane of the figure. (top) Contours of along-streak velocity. (bottom) Contours of the streamfunction of the circulation in an across-streak plane. Contours are regularly spaced. The across-streak coordinate $\mathbf{x} \cdot \mathbf{k}/k$ is normalized by the PBL height $H = 750$ m.

At this point it is useful to emphasize the difference in horizontal and vertical scales between the SL structures considered here and the PBL structures studied by Wilson (1996). Wilson classifies the EOFs extracted from the LES of a slightly convective PBL in several categories: random motion, motion near the inversion layer, thermal, and longitudinal roll. The latter structure, labeled E1 in Wilson (1996), spans most of the PBL and has a horizontal wavelength comparable to the PBL depth. At contrast, the flow displayed in Fig. 6 spans about 20% of the PBL and its wavelength is one-third of the PBL depth. Furthermore, it is one of the largest modes among the strongly structured modes lying on the line $3k_x + k_y = 0$; the other ones (not dis-

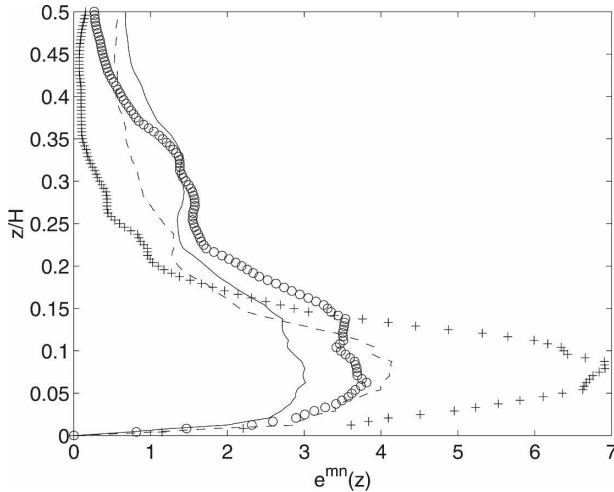


FIG. 7. Vertical repartition $E^1(m, n, z)$ of the kinetic energy of the first EOFs for Fourier modes $-m = n = 2$ (circles) and $-m = n = 4$ (crosses). Vertical repartition E^{mn} of the total kinetic energy contained in the Fourier modes $-m = n = 2$ (solid) and $-m = n = 4$ (dashed). These quantities are adimensional and their vertical integral is equal to one. The corresponding horizontal scale is $\lambda = 474$ m ($-m = n = 2$) and $\lambda = 237$ m ($-m = n = 4$), respectively.

played) are of smaller scale in both the vertical and horizontal directions.

We finally display for the Fourier modes $-m = n = 2$ and $-m = n = 4$ the vertical profiles of kinetic energy $E^1(m, n, z)$ (Fig. 7) and of production rate of energy by the shear $S^1(m, n, z)$ (Fig. 8). Because of the normalization of the EOFs, $E^1(m, n, z)$ is an adimensional quantity whose vertical integral is 1. It can be seen that the energy of the first EOF is concentrated closer to the ground than the total energy of the corresponding Fourier mode. Concerning the shear production, most of it is solely due to the first EOF. Only very close to the ground does the flux intensity contributed by the first EOF decrease much faster than the total contribution by the corresponding Fourier mode. The maximum shear production for the first EOF of Fourier mode ($-m = n = 4$) is attained at an altitude $\approx 0.08H$ (i.e., about 60 m), which corresponds to the typical altitude up to which streaks can be observed on horizontal cross sections of this LES.

4. Contribution to turbulence anisotropy

Here, as in previous studies (Rinker and Young 1996; Wilson 1996; Finnigan and Shaw 2000; Esau 2003), the EOF technique proves successful at (i) identifying the horizontal characteristics of the energetic flow patterns (wavelength and orientation) and (ii) providing the corresponding vertical structure of the flow. We now pro-

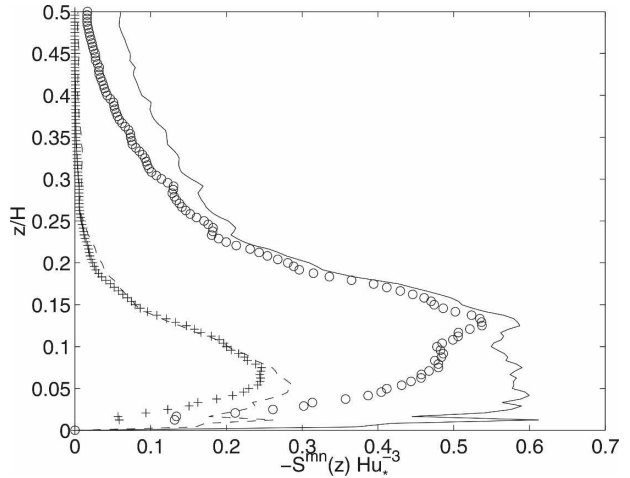


FIG. 8. Vertical profile of $-S^1(m, n, z)$ (contribution of the first EOFs to the shear production; see section 2c) for Fourier modes $-m = n = 2$ (circles) and $m = -n = 4$ (crosses). Vertical profile of the total shear production S^{mn} for the Fourier modes $-m = n = 2$ (solid) and $-m = n = 4$ (dashed).

ceed with the analysis of the contribution of these structures to turbulence anisotropy. Strictly speaking, this analysis is independent from the previous discussion. However the line $3k_x + k_y$ will be a useful visual guide emphasizing where strongly structured modes are located in the spectral domain. Meanwhile it must be borne in mind that the energetic patterns extracted by the EOF technique represent only a small fraction of the energy (except, by construction, in the strongly structured spectral domain).

a. Vertical extent

The vertical extent of rolls or streaks is often studied by investigating up to which height above ground the spatial features of a horizontal cross section ($z = \text{const}$) of the velocity field survive. Here, because the EOFs precisely represent the correlations between the different altitudes, the different levels are never considered independently. Therefore we characterize the vertical extent of the turbulent structures through their TKE center, the column average of altitude weighted by the turbulent kinetic energy (Wilson 1996):

$$Z(m, n) = \frac{\int z E(m, n, z) dz}{\int E(m, n, z) dz}, \tag{28}$$

$$Z^1(m, n) = \frac{\int z E^1(m, n, z) dz}{\int E^1(m, n, z) dz}. \tag{29}$$

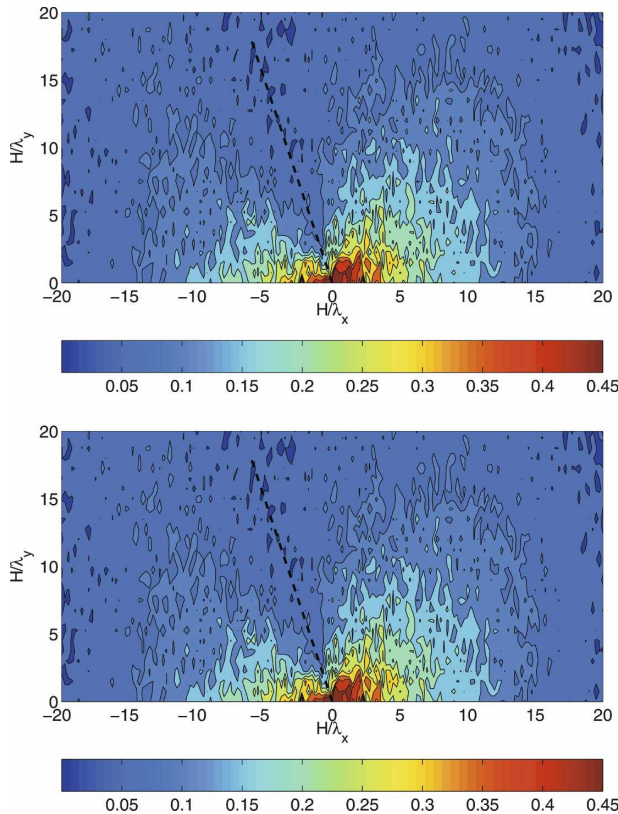


FIG. 9. TKE center $Z^1(m, n)/H$ normalized by the PBL height $H = 750$ m, as a function of the normalized horizontal wave vector $H\mathbf{k}/2\pi = (H/\lambda_x, H/\lambda_y)$. The black, dashed line $3k_x + k_y = 0$ emphasizes the strongly structured region of Fourier space found in section 3.

In this definition, we can choose to weigh by the TKE $E(m, n, z) = \langle e(m, n, z, t) \rangle$ at altitude z and wavenumber (m, n) or only by the contribution $E^1(m, n, z)$ of the first EOF. In addition, we may consider the total TKE or only the horizontal TKE $E_H = \frac{1}{2}\langle u^2 + v^2 \rangle$ or the vertical TKE $E_V = \frac{1}{2}\langle w^2 \rangle$. The height $Z(m, n)$ can then be interpreted as a penetration height up to which a given Fourier mode or EOF contributes significantly to the horizontal Fourier spectrum.

We display in Fig. 9 the TKE center as a function of the horizontal wavenumber, obtained from the horizontal energy $E_H(m, n, z)$ of the corresponding Fourier mode (Fig. 9a) or obtained from the horizontal energy $E_H^1(m, n, z)$ of the corresponding first EOF only (Fig. 9b). A global trend is that horizontally short structures (large wave vectors) have a correspondingly small vertical extent. A striking feature is the strong anisotropy in the values of the TKE center Z . For wave vectors lying on the line $3k_x + k_y = 0$, the TKE center is much smaller than that of wave vectors of comparable magnitude and different direction. This anisotropy is more

pronounced for the TKE center based on EOFs (Fig. 9b). The line $3k_x + k_y = 0$ corresponds to the strongly structured wave vectors. Hence what we observe is that the most energetic patterns of this flow are more concentrated close to the ground than motions of comparable horizontal scale for which no significant EOF can be extracted, indicating more disordered motion.

Considering, finally, the TKE center obtained now from the vertical energy $E_V(m, n)$ (not shown), the trend that horizontally short structures have a small vertical extent persists. However, the anisotropy in the values of the TKE center Z_{mm} is much less apparent, yet still visible for the TKE center based on EOFs. Now, the vertical velocity is blocked near the ground, which is not the case for the horizontal components. The strength of this blocking effect does not depend on the direction of the wave vector. Hence it may be the origin of the weaker dependence of the vertical TKE on the direction of the horizontal wave vector.

b. Vertical versus horizontal turbulent kinetic energy

We have discussed so far the anisotropic dependence of the vertical extent of flow patterns on their horizontal wave vector. Anisotropy may enter in a second way for a vector quantity such as velocity, since it may point in directions that are not isotropically distributed. An indication of that is given by the ratio E_V/E_H of the vertical TKE over the horizontal TKE. The properties of homogeneous and isotropic turbulence are that (i) the ensemble means associated with the turbulent state are invariant with respect to any translation, rotation, or symmetry; and (ii) in practice, there is no privileged direction for turbulence. If the velocity fluctuations had isotropically distributed directions, as in locally isotropic turbulence, we would have $\langle u^2 \rangle = \langle v^2 \rangle = \langle w^2 \rangle$ and the ratio E_V/E_H would be equal to one-half.

We display in Fig. 10a the TKE ratio E_V/E_H as a function of the horizontal wavenumber. Only for very small scales (large wave vectors) does E_V/E_H approach the isotropic value of one-half. Everywhere else the TKE ratio is in favor of the horizontal TKE, especially at large horizontal scales (small wave vectors) but also and more remarkably for strongly structured wave vectors (lying on the line $3k_x + k_y = 0$). Figure 10b presents the ratio E_V^1/E_H^1 of the contribution of the first EOF to the vertical and horizontal TKEs. Retaining only the first EOFs worsens the statistical convergence, resulting in a noisier plot. Nevertheless, the features discussed above are clearly visible in an even more pronounced way. In a narrow angular sector containing the strongly structured line $3k_x + k_y = 0$, the TKE ratio is

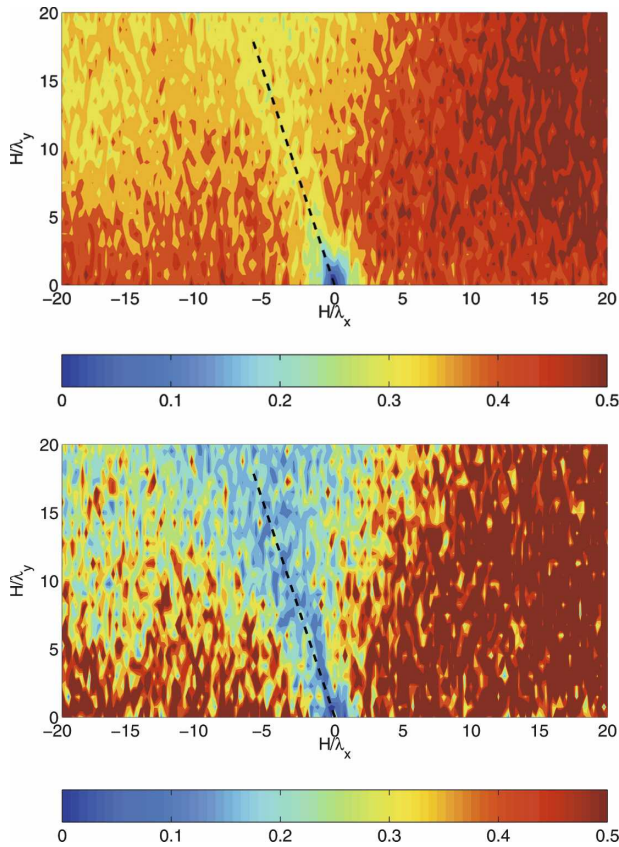


FIG. 10. Ratio E_V/E_H of vertical to horizontal TKE as a function of the horizontal wave vector $\mathbf{k} = (k_x, k_y) = (2\pi/\lambda_x, 2\pi/\lambda_y)$ normalized by the PBL height $H = 750$ m. (a) Vertically averaged TKEs. (b) Only the contribution due to the first EOF. The black, dashed line $3k_x + k_y = 0$ indicates the strongly structured region of Fourier space. The black, dashed line $3k_x + k_y = 0$ emphasizes the strongly structured region of Fourier space found in section 3.

in favor of the horizontal TKE while it is much closer to its isotropic value of one-half outside this sector.

It is expected that isotropy is violated by structures with very large horizontal scale since their vertical extent is limited by the PBL height, resulting in a low geometric aspect ratio. Because of incompressibility, such structures with small vertical extent relative to their horizontal scale have a correspondingly low vertical velocity. Conversely, horizontally short structures are free to achieve a vertical–horizontal aspect ratio of 1 or more and the corresponding ratio of vertical to horizontal TKE. This is clearly not the case at strongly structured wave vectors for which a typical e_V/e_H ratio is about 0.2 even at large wave vectors. This is consistent with the observation that the corresponding flow patterns are closer to the ground than those of equivalent horizontal scale and different direction, resulting in a lower vertical–horizontal aspect ratio. Noticing from Fig. 3 that, for the total signal, $\langle v^2 \rangle / \langle u^2 \rangle$ and $\langle w^2 \rangle / \langle v^2 \rangle$

are about 0.5, we obtain that $E_V/E_H \approx 0.17$, which is remarkably similar to the ratio found for the strongly structured wave vectors. Hence the strongly structured wave vectors carry a turbulence anisotropy that is representative of the anisotropy observed in the total signal.

5. Summary

We have analyzed a dataset produced by a LES of a neutral atmospheric surface layer (SL). In the LES, the small-scale streaks can be observed up to about $0.13H$ (i.e., 100 m above the ground). We have performed an empirical orthogonal function (EOF) analysis; this method exploits the statistical information contained in the self-correlation matrix [Eq. (4)], here the correlations between the velocity fluctuations at different altitudes (10). This is in contrast to, for instance, a level-by-level spectral analysis, which would discard these correlations.

Not all horizontal wave vectors, rather few in fact, present distinct patterns in their vertical profile. We identified the narrow band in the Fourier space near $3k_x + k_y = 0$ where such energetic patterns are strong enough that the first EOF carries more energy than the next ones altogether. The orientation of this band is in agreement with a level-by-level identification of the streak lines. Thus these streak patterns are indeed produced by structures with a spatial coherence on the vertical. Furthermore, the extracted EOFs have a flow structure similar to that of linearly unstable normal modes and optimal perturbations. EOF analysis thus provides a way to compare features emerging from complex, fully nonlinear dynamics and idealized, linearized dynamics. From this comparison, it turns out that the flow patterns of coherent structures bear more resemblance to the optimal perturbations (Foster 1997) than to the unstable normal modes (Lilly 1966).

Foster et al. (2006) analyze the same dataset using level-by-level spectral analysis and conditional sampling, focusing on the relationship between streaks, upward ejections of low-momentum air, and downward sweeps of high-momentum air. Conditional sampling does not separate the various horizontal scales of the velocity fluctuations; conversely, EOF analysis does not distinguish between ejections and sweeps. This makes the two methods complementary in that they focus on different issues. Nevertheless, both EOF analysis and level-by-level spectral analysis provide length scales for the streaks. Foster et al. (2006) find that the streaks present multiple horizontal scales, ranging from 125 to 264 m at the lowest level. They also observe that the large-scale peaks disappear farther from the surface

than small-scale peaks. This is consistent with our result that the EOFs computed at larger horizontal wave vectors have a smaller vertical extension.

Beyond the extraction and identification of coherent structures, we further analyze their contribution to the turbulence anisotropy, which is the main aim of this work. The EOF analysis helps us in two ways in this task. First, it points us at the regions of Fourier space where coherent structures are important and might have a signature on the turbulence. We find that two characteristics of the turbulence anisotropy depend on whether the velocity fluctuations with a given horizontal wave vector present distinct patterns:

- 1) The turbulence extends on a vertical range much smaller for structured wave vectors than for unstructured wave vectors with comparable magnitude and unspecified direction. This observation is particularly true for the fluctuations of horizontal velocity (as measured by the horizontal turbulent kinetic energy) and less for vertical velocity.
- 2) The velocity fluctuations themselves are also distributed in a less isotropic way, as made apparent by the depleted ratio of vertical and horizontal turbulent kinetic energies.

Second, EOF analysis not only extracts coherent structures but also separates the velocity field into its projection onto the dominant EOFs and remaining, less structured fluctuations. The above two anisotropies of turbulence are strongly emphasized when the signal is projected onto the most energetic EOF of each Fourier mode. This indicates that the coherent structures do indeed “carry” more anisotropy than the remaining turbulent fluctuations. Notice that the above two anisotropies of turbulence are convincingly present in the complete signal. This is important since the dominant EOFs finally account for a relatively small fraction of the total kinetic energy, and the significance of properties of the EOF-filtered signal could therefore be questionable. Hence we rely on both the EOF-filtered signal and the complete signal to characterize the signature of the coherent structures on anisotropy, which we find indeed significant.

We did not discuss the flow pattern produced by the second EOF. Notice that the statistical convergence of the higher EOFs (not investigated here) may require a larger dataset. Furthermore, the flow patterns present several recirculation loops and are not easy to interpret. This is a manifestation of the general rule that higher EOFs cannot be interpreted individually but only in combination with the previous ones (Berkooz et al. 1993). They may deserve additional investigations.

In terms of parameterization, implementing subgrid-

scale models that conceptually account for the contribution of the coherent structures to near-surface energetics remains an issue. Improvements have been made on the subgrid representation of coherent structures to the total momentum and heat fluxes (Foster and Brown 1994; Redelsperger et al. 2001; Hourdin et al. 2002; Drobinski et al. 2006) but not to the directional kinetic energy and dissipation. Even though this is not treated as such in this article, we believe it is worth to emphasize this issue. Finally, while neutral stratification is an important dynamical regime, nonneutral stratification substantially affects the coherent structures and probably their contribution to the turbulence anisotropy. Future works will investigate this contribution in the stably stratified PBL, where both the structure of turbulence and the dynamics of coherent structures are less well understood than in the convective PBL.

Acknowledgments. The authors thank J.-L. Redelsperger, H. Adanfari, and R. C. Foster for fruitful discussions; and M. C. Lanceau for help in collecting the referenced papers. The LES was done thanks to a funding of the French Ministry for Transportation and Météo France. This research has also been funded by the Centre National de Recherche Scientifique (CNRS) and the Institut des Sciences de l’Univers (INSU) through the Programme Atmosphère Océan à Multi-échelle (PATOM).

REFERENCES

- Andren, A., A. Brown, J. Graf, P. Mason, C. Moeng, F. Nieuwstadt, and U. Schumann, 1994: Large-eddy simulation of a neutrally stratified boundary layer: A comparison of 4 computer codes. *Quart. J. Roy. Meteor. Soc.*, **120**, 1457–1484.
- Berkooz, G., P. Holmes, and J. Lumley, 1993: The proper orthogonal decomposition in the analysis of turbulent flows. *Annu. Rev. Fluid Mech.*, **25**, 539–575.
- Carloti, P., 2002: Two-point properties in atmospheric turbulence very close to the ground: Comparison of a high resolution LES with theoretical models. *Bound.-Layer Meteor.*, **104**, 381–410.
- , and P. Drobinski, 2004: Length scales in wall-bounded high-Reynolds-number turbulence. *J. Fluid Mech.*, **516**, 239–264.
- Cuxart, J., P. Bougeault, and J.-L. Redelsperger, 2000: A multi-scale turbulence scheme apt for LES and mesoscale modeling. *Quart. J. Roy. Meteor. Soc.*, **126**, 1–30.
- Deardorff, J. W., 1972: Numerical investigation of neutral and unstable planetary boundary layers. *J. Atmos. Sci.*, **29**, 91–115.
- Drobinski, P., and R. Foster, 2003: On the origin of near-surface streaks in the neutrally-stratified planetary boundary layer. *Bound.-Layer Meteor.*, **108**, 247–256.
- , R. Brown, P. Flamant, and J. Pelon, 1998: Evidence of organized large eddies by ground-based Doppler lidar, sonic anemometer and sodar. *Bound.-Layer Meteor.*, **88**, 343–361.
- , P. Carloti, R. Newson, R. Banta, R. Foster, and J.-L. Re-

- delserperger, 2004: The structure of the near-neutral atmospheric surface layer. *J. Atmos. Sci.*, **61**, 699–714.
- , J.-L. Redelsperger, and C. Pietras, 2006: Evaluation of a planetary boundary layer subgrid-scale model that accounts for near-surface turbulence anisotropy. *Geophys. Res. Lett.*, **33**, L23806, doi:10.1029/2006GL027062.
- , P. Carlotti, J.-L. Redelsperger, R. Banta, V. Masson, and R. Newsom, 2007: Numerical and experimental investigation of the neutral atmospheric surface layer. *J. Atmos. Sci.*, **64**, 137–156.
- Esau, I., 2003: The Coriolis effect on coherent structures in planetary boundary layers. *J. Turbul.*, **4**, 17.
- Etling, D., and R. Brown, 1993: Roll vortices in the planetary boundary layer: A review. *Bound.-Layer Meteor.*, **65**, 215–248.
- Finnigan, J. J., and R. H. Shaw, 2000: A wind-tunnel study of airflow in waving wheat: An EOF analysis of the structure of the large-eddy motion. *Bound.-Layer Meteor.*, **96**, 211–255.
- Foster, R. C., 1997: Structure and energetics of optimal Ekman layer perturbations. *J. Fluid Mech.*, **333**, 97–123.
- , and R. A. Brown, 1994: On large-scale PBL modelling: Surface wind and latent heat flux comparisons. *Global Atmos. Ocean Syst.*, **2**, 199–219.
- , F. Vianey, P. Drobinski, and P. Carlotti, 2006: Near-surface coherent structures and the vertical momentum flux in a large-eddy simulation of the neutrally-stratified boundary layer. *Bound.-Layer Meteor.*, **120**, 229–255.
- Grant, A. L. M., 1986: Observations of boundary layer structure made during the 1981 KONTUR experiment. *Quart. J. Roy. Meteor. Soc.*, **112**, 825–841.
- , 1992: The structure of turbulence in the near-neutral atmospheric boundary layer. *J. Atmos. Sci.*, **49**, 226–239.
- Hess, G. D., 2004: The neutral, barotropic planetary boundary layer, capped by a low-level inversion. *Bound.-Layer Meteor.*, **110**, 319–355.
- Holmes, P., J. Lumley, and G. Berkooz, 1996: *Turbulence, Coherent Structures, Dynamical Systems, and Symmetry*. Cambridge University Press, 420 pp.
- Holtslag, A., and F. Nieuwstadt, 1986: Scaling the atmospheric boundary layer. *Bound.-Layer Meteor.*, **36**, 201–209.
- Hourdin, F., F. Couvreux, and L. Menut, 2002: Parameterization of the dry convective boundary layer based on a mass flux representation of thermals. *J. Atmos. Sci.*, **59**, 1105–1123.
- Hunt, J. C. R., and J. Morrison, 2000: Eddy structure in turbulent boundary layers. *Eur. J. Mech.*, **19B**, 673–694.
- , and P. Carlotti, 2001: Statistical structure at the wall of the high Reynolds number turbulent boundary layer. *Flow Turbul. Combust.*, **66**, 453–475.
- Jallicee, J., and C. Ropelewski, 1979: An objective analysis of the boundary-layer thermodynamic structure during GATE. Part I: Method. *Mon. Wea. Rev.*, **107**, 68–76.
- Jeong, J., and F. Hussain, 1995: On the identification of a vortex. *J. Fluid Mech.*, **285**, 69–94.
- Katul, G., and C.-R. Chu, 1998: A theoretical and experimental investigation of energy-containing scales in the dynamic sub-layer of boundary-layer flows. *Bound.-Layer Meteor.*, **86**, 279–312.
- Lafore, J., and Coauthors, 1998: The Meso-NH Atmospheric Simulation System. Part I: Adiabatic formulation and control simulations. *Ann. Geophys.*, **16**, 90–109.
- Lilly, D., 1966: On the instability of Ekman boundary flow. *J. Atmos. Sci.*, **23**, 481–494.
- Lin, C.-L., J. McWilliams, C.-H. Moeng, and P. Sullivan, 1996: Coherent structures and dynamics in a neutrally-stratified planetary boundary layer flow. *Phys. Fluids*, **8**, 2626–2639.
- Moeng, C.-H., and P. P. Sullivan, 1994: A comparison of shear- and buoyancy-driven planetary boundary layer flows. *J. Atmos. Sci.*, **51**, 999–1022.
- Nicholls, S., and C. Readings, 1979: Aircraft observations of the structure of the lower boundary layer over the sea. *Quart. J. Roy. Meteor. Soc.*, **105**, 785–802.
- Panofsky, H. A., 1974: The atmospheric boundary layer below 150 meters. *Annu. Rev. Fluid Mech.*, **6**, 147–177.
- Preisendorfer, R., 1988: *Principal Component Analysis in Meteorology and Oceanography*. Elsevier, 425 pp.
- Redelsperger, J.-L., F. Mahé, and P. Carlotti, 2001: A simple and general subgrid model suitable both for surface layer and free-stream turbulence. *Bound.-Layer Meteor.*, **101**, 375–408.
- Rinker, D. K., and G. Young, 1996: Use of obliquely rotated principal component analysis to identify coherent structures. *Bound.-Layer Meteor.*, **80**, 19–47.
- Smagorinsky, J., 1963: General circulation experiments with the primitive equations. I. The basic experiment. *Mon. Wea. Rev.*, **91**, 99–164.
- Wilson, D. K., 1996: Empirical orthogonal function analysis of the weakly convective atmospheric boundary layer. Part I: Eddy structures. *J. Atmos. Sci.*, **53**, 801–823.
- , and J. C. Wyngaard, 1996: Empirical orthogonal function analysis of the weakly convective atmospheric boundary layer. Part II: Eddy energetics. *J. Atmos. Sci.*, **53**, 824–841.
- Young, G., D. Kristovich, M. Hjelmfelt, and R. Foster, 2002: Rolls, streets, waves, and more: A review of quasi-two-dimensional structures in the atmospheric boundary layer. *Bull. Amer. Meteor. Soc.*, **83**, 997–1001.